Surface & Coatings Technology 254 (2014) 238–243

Contents lists available at ScienceDirect

Surface & Coatings Technology

journal homepage: www.elsevier.com/locate/surfcoat

Corrosion properties of Fe–Cr–Nb–B amorphous alloys and coatings

G.Y. Koga [a], R.P. Nogueira [b], V. Roche [b], A.R. Yavari [c], A.K. Melle [a], J. Gallego [d], C. Bolfarini [a], C.S. Kiminami [a], W.J. Botta [a,*]

[a] Universidade Federal de São Carlos, Departamento de Engenharia de Materiais, Rod. Washington Luis, km 235, CEP 13565-905 São Carlos, SP, Brazil
[b] LEPMI, UMR5279 CNRS, Grenoble INP, Université de Savoie, Université Joseph Fourier, 1130, rue de la piscine, BP 75, 38402 Saint Martin d'Hères, France
[c] SIMaP, CNRS, Institut National Polytechnique, Grenoble INP, 1130 rue de la Piscine, 38402 Saint-Martin-d'Hères, France
[d] Universidade Estadual Paulista, Departamento de Engenharia Mecânica, Avenida Brasil Centro, CEP 15385-000, Ilha Solteira, SP, Brazil

ARTICLE INFO

Article history:
Received 23 January 2014
Accepted in revised form 13 June 2014
Available online 20 June 2014

Keywords:
Corrosion
Coating
Amorphous
Steel

ABSTRACT

In the present work, we report on the corrosion properties of the $Fe_{60}Cr_8Nb_8B_{24}$ (at.%) alloy produced using pure and commercial materials in the following conditions: amorphous ribbons, partially crystallized ribbons and coatings produced by spray deposition and powder flame spraying process, in this case LVOF (low velocity oxygen fuel). The amorphous ribbons showed excellent corrosion resistance with formation of a stable passive film that ensured a very large passivation plateau. The (LVOF) coatings presented high fraction of amorphous phase with a layered structure, high porosity (16.2%) and low oxidation level (~0.1%). The spray formed coatings presented crystalline structure with low porosity (1.9%) and low oxidation level (~0.1%). The coatings showed higher corrosion current densities (up to two orders of magnitude) compared to the amorphous ribbons of the same composition for all pH. This deterioration in the corrosion properties were found to be impaired by the presence of crystalline phases.

1. Introduction

Fe-based amorphous alloys can be designed to present an attractive combination of properties which include high mechanical strength, high corrosion and wear resistance, good magnetic properties and in addition, they are relatively low cost materials [1–3].

These alloys can be obtained in the amorphous state by different rapid solidification processes such as melt spinning, gas atomization, spray deposition, and high-energy ball milling. Powder alloys can then be used to produce amorphous coatings on steel substrate, improving corrosion properties in aggressive environments [4,5], such as chemical industries and oil refineries.

The use of conventional commercial alloys to produce lower cost coatings is certainly of interest but it is clearly dependent on composition modification to allow amorphization during rapid solidification processing. Bulk Fe-based amorphous alloys have already been obtained from FC20 cast iron, from 430 SS stainless steel or even by the use of commercial grade elements such as Fe–P and Fe–B [6–8].

Coatings from these alloys have also been obtained by different processes, such as thermal spraying, laser cladding and so on, and there are important differences between the processes concerning retention of a fully amorphous structure, stability and adhesion of the coated layer to the substrate [9–13].

The relatively high corrosion resistance of the amorphous phase as compared to the equivalent crystalline material [14–16] can be attributed to the higher chemical homogeneity and typical absence of crystallographic imperfections such as grains, grain boundaries, second phase elements and dislocations or segregations which are more susceptible to chemical attack [17,18].

The corrosion behaviors of many different Fe-based amorphous alloy compositions have already been studied [19–28]. In the FeCuNbSiB system, for the compositions $Fe_{77.5}Cu_1Nb_3Si_{2.5}B_{16}$, $Fe_{74}Cu_1Nb_3Si_{13.5}B_{8.5}$, $Fe_{73}Cu_1Nb_3Si_{15.5}B_{7.5}$ and $Fe_{73}Cu_1Nb_3S_{16.5}B_{6.5}$ the increase in the Si content increased the corrosion resistance both for the amorphous and the nanocrystalline states [19]. But for this and for many other systems, as for example, for the alloys $Fe_{84}Nb_7B_9$, $Fe_{84}Zr_7B_9$, and $Fe_{83}Zr_{3.5}Nb_{3.5}B_9Cu_1$ [22], the presence of crystalline phases always decreased the corrosion resistance. Compositions containing Cr, Nb and Mo generally present improved corrosion properties due to the spontaneous passivation of the alloys. Comparison of the corrosion properties for the $Fe_{68}B_{20}Cr_{12}$, $Fe_{67.7}B_{20}Cr_{12}Mo_{0.3}$, $Fe_{67.7}B_{20}Cr_{12}Nb_{0.3}$ and $Fe_{67.7}B_{20}Cr_{12}Nb_{0.15}Mo_{0.15}$ alloys indicated that the presence of Mo and/or Nb increased the uniform corrosion resistance and the pitting corrosion resistance, which was further enhanced by the presence of both elements [26].

In the present study we evaluated the corrosion resistance of the $Fe_{60}Cr_8Nb_8B_{24}$ (at.%) alloy in the following conditions: amorphous ribbons, partially crystallized ribbons and coatings over mild steel subtract produced by spray deposition and powder flame spraying process. The

* Corresponding author.
E-mail address: wjbotta@ufscar.br (W.J. Botta).

http://dx.doi.org/10.1016/j.surfcoat.2014.06.022
0257-8972/

corrosion resistance was evaluated in chloride-rich media in different pH (3.0, 5.5 and 10.0).

2. Experimental procedure

The $Fe_{60}Cr_8Nb_8B_{24}$ (at.%) alloy belongs to a family of quaternary Fe-based alloys developed primarily from industrial grade materials to present good glass forming ability [8]. The alloy used in our work was prepared using a ferritic stainless steel (FSS) AISI 430 with high Cr content, combined with additions of Fe–Nb and Fe–B master alloys as raw materials (Table 1). The nominal composition was finally adjusted by adding pure electrolytic Fe (99.5%) and pure Nb (99.9%) elements.

Amorphous $Fe_{60}Cr_8Nb_8B_{24}$ (at.%) ribbons were produced by melt spinning with copper wheel rotating at a speed of 50 m s^{-1} in an argon atmosphere. Annealing treatments were conducted in short time annealing (60 s) under controlled atmosphere at the following temperatures: 450, 550 and 640 °C.

Coatings over commercial AISI 1010 steel substrates were produced using two different routes: spray deposition and powder flame spraying, in this case, low velocity oxygen fuel (LVOF). The spray forming process was carried out under nitrogen gas and the sprayed powder hit directly the substrate, which was placed away from the central deposit area to ensure deposition from the smallest particle size range. For the LVOF process, atomized powders with spherical morphology in the size range <45 μm were used. Table 2 summarizes the spraying parameters.

The microstructure and chemical characterization of the coatings were examined by scanning electron microscopy (SEM), Philips XL30 FEG and energy dispersive spectroscopy (EDS). The ribbons were characterized by transmission electron microscopy (TEM) in a FEI Tecnai G^2 200 kV. X-ray diffraction (XRD) analysis of all specimens was performed on an X-ray diffractometer Rigaku Geigerflex ME210GF2, with Cu-Kα radiation. The thermal stability was examined by differential scanning calorimeter (DSC), Netzsch 404, at a heating rate of 0.67 K/s. Percentage of the porosity in the coatings was evaluated using image analysis (AnalySIS Pro) on an optical microscopy ZEISS and the oxygen content was measured using a LECO TC-436 DR apparatus. Topography analysis of the samples were performed after the electrochemical tests, in an optical microscope (OM) Leitz Laborlux 12ME S, Leica.

The corrosion behavior of the ribbons and coatings was evaluated by the corrosion current density (I_{corr}) and the corrosion potential (E_{corr}) obtained from polarization curves. Reproducibility of data was ensured by repeating the tests at least two times. Corrosion current density values, I_{corr}, were determined by extrapolating the anodic and cathodic Tafel regions on the potentiodynamic results around E_{corr} with the intersection being considered as I_{corr}.

The polarization curves were measured using a three electrode cell set-up; the working electrodes were the amorphous and annealed ribbons as well as the coatings of the same composition, the counter electrode was a platinum foil (Pt) and a saturated calomel electrode (SCE) was used as the reference.

Each test was carried out in the following three conditions to simulate chloride-rich environment (Cl^- content equivalent to sea water concentration) at different pH to track the corrosion behavior at acidic and alkaline chloride media: (i) deionized water, 35 g/L of NaCl and addition of H_2SO_4 until pH = 3.0; (ii) deionized water, 35 g/L of NaCl and addition of H_2SO_4 until pH = 5.5 and (iii) deionized water, 35 g/L of NaCl and addition of NaOH until pH = 10.0.

Table 2
Detailed parameters used during spray deposition process and LVOF flame spray, respectively.

Spray deposition process	
Gas flow rate – N_2 (m^3/min)	3.84
Mass flow rate (kg/min)	5.56
Gas to metal rate – G/M (m^3/kg)	0.69
Temperature (°C)	1600
Nozzle diameter (mm)	6
Deposit thickness (mm)	5
Low velocity oxygen fuel (LVOF)	
Powder sizes (μm)	<45
Spraying distance (mm)	100
Acetylene (psi)	35
Oxygen (psi)	75
Coating thickness (μm)	200

For comparison purposes, electrochemical analyses were also carried out under the same conditions on an austenitic stainless steel 316L, well-known to show very high corrosion resistance in the tested media as well as on an AISI 430 stainless steel, which was the master alloy used for the production of the ribbons and coatings of the $Fe_{60}Cr_8Nb_8B_{24}$ alloy. Table 3 shows the chemical composition of the stainless steel 316L.

3. Results and discussion

Fig. 1 shows the XRD patterns of the different samples evaluated in this work; amorphous ribbons and ribbons annealed at the indicated temperatures, and the coatings produced by LVOF and spray deposition.

The XRD pattern for the as-spun samples consists only of a broad halo associated with the amorphous structure. No diffraction peak due to crystalline phase is seen in the ribbons annealed at 450 °C and 550 °C, but clear peaks related to crystalline phases is recognized for the sample annealed at 640 °C. The coatings obtained by LVOF show high fraction of amorphous phases, but some sharp diffraction peaks superimposed on a broad halo pattern were observed, indicating formation of a mixture of amorphous and crystalline Fe-α, Fe_2B and FeNbB phases. The spray deposition process produced completely crystalline coatings containing Fe-α, Fe_2B and FeNbB phases.

Fig. 2 shows the DSC curves for the same set of samples; as-spun and annealed ribbons at the indicated temperatures and coatings obtained by LVOF and spray deposition process. The curves corresponding to the amorphous and to the samples annealed at 450 °C and 550 °C exhibit two exothermic peaks corresponding to different stages of crystallization and show clear glass transition temperature (T_g) which is indicated in the figure together with T_x, the crystallization temperature. From the values of T_g and T_x (for the first crystallization peak), we obtain the supercooled liquid range ΔT_x ($\Delta T_x = T_x - T_g$) of 60 K for the as-spun ribbon indicating high thermal stability of the supercooled liquid against the crystallization, also suggesting high glass forming ability for this alloy. The ribbons annealed at 640 °C and the coatings produced by LVOF process show a crystallization peak related to the amorphous phase fraction.

Table 1
Chemical composition of precursor materials: FSS 430, Fe–B and Fe–Nb master alloys and the nominal composition for the FeCrNbB alloy (in this case in wt.%, for comparison with the commercial materials).

	C	Si	Mn	Cr	Ni	S	P	Mo	Nb	Co	N	B	Fe
AISI 430	0.057	0.2	0.74	17.62	0.37	0.17	0.025	0.06	0.03	0.03	0.031	–	Bal.
Fe–B	0.3	0.57	–	–	–	–	–	–	–	–	–	16.5	Bal.
Fe–Nb	0.2	3.0	–	–	–	0.1	0.2	–	63	–	–	–	Bal.
FeCrNbB	0.157	0.91	0.29	8.03	0.14	0.09	0.054	0.02	14.51	0.01	0.012	5.45	Bal.

Table 3
Chemical composition (wt.%) of stainless steel 316L.

	C	Si	Mn	Ni	Cr	Mo	N	Al	Fe
316L SS	0.028	0.571	1.018	11.995	18.003	2.989	0.029	0.0036	Bal.

Fig. 3a, b and c show, respectively, the microstructure of the coatings produced by LVOF and spray deposition routes. In Fig. 3a a layered structure and a high volume fraction of irregular porosity (16.2%) can be observed. Fig. 3b and c shows a dense coating (porosity = 1.9%) produced by spray deposition and the presence of a high fraction of FeNbB phase. The coatings obtained by both routes presented low oxidation levels (~0.1%). Microanalysis in three selected locations (1, 2 and 3) in Fig. 3a and c confirms the presence of a Nb-enriched phase and two phases rich in Fe and poor in Nb. The concentration of light element such as B could not be determined by EDS but, as identified by XRD, the phases are most likely FeNbB, Fe_2B and Fe-α.

The bright-field (BF) transmission electron micrograph and the selected area electron diffraction pattern of the as-spun and annealed ribbons are shown in Fig. 4. The bright-field images for the ribbons annealed at 450 °C and 550 °C (Fig. 4a and b, respectively) reveal no appreciable contrast corresponding to crystalline phase and in addition the respective electron diffraction patterns consist only of halo rings, characteristics of amorphous structure. The bright-field image and the electron diffraction patterns as shown in Fig. 4c reveal a typical amorphous matrix and some black and gray nanosized crystalline phases embedded within the matrix, corresponding to the partial crystallization of the ribbons annealed at 640 °C. The selected area diffraction pattern indicates that the phases formed after partial crystallization correspond to the α-Fe, FeB and Fe_3B.

Fig. 5 shows the polarization curves for the $Fe_{60}Cr_8Nb_8B_{24}$ amorphous and annealed ribbons as well as for the two coatings produced with the same composition (spray deposition and LVOF) in the chloride-rich pH = 5.5 electrolyte. For the sake of comparison, Fig. 5 also shows results for the commercial FSS 430, the master alloy from which all of the samples were prepared and those from the 316L stainless steel which is known to present outstanding corrosion properties. Polarization curves obtained at acid and alkaline conditions were qualitatively quite similar to those in Fig. 5 for all the samples and are hence not shown here. The ensemble of results is summarized in Table 4 for all pH conditions.

Two different corrosion behaviors are observed regardless of the pH. It clearly appears that the fully amorphous ribbons, including the ribbons annealed at 450 °C and 550 °C, have a much better corrosion resistance (lower corrosion current density and more noble corrosion potential) than the ferritic stainless steel in the different media regardless of the pH. Indeed, depending on the pH, the amorphous ribbons showed corrosion resistance even higher (lower current densities) than that of the 316L SS.

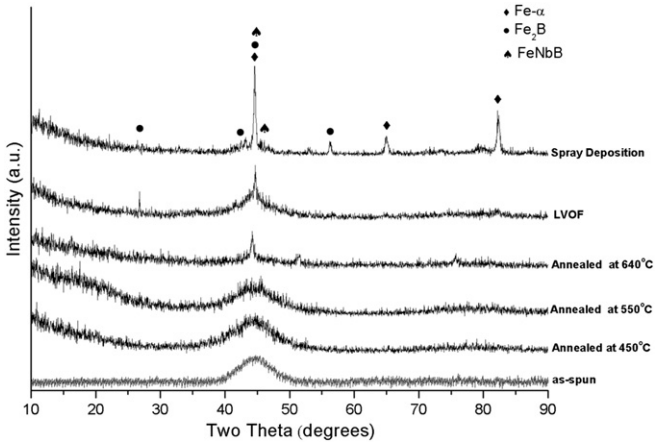

Fig. 1. XRD patterns for the $Fe_{60}Cr_8Nb_8B_{24}$ as-spun ribbons, annealed ribbons at the indicated temperatures and coatings obtained by LVOF and spray deposition routes.

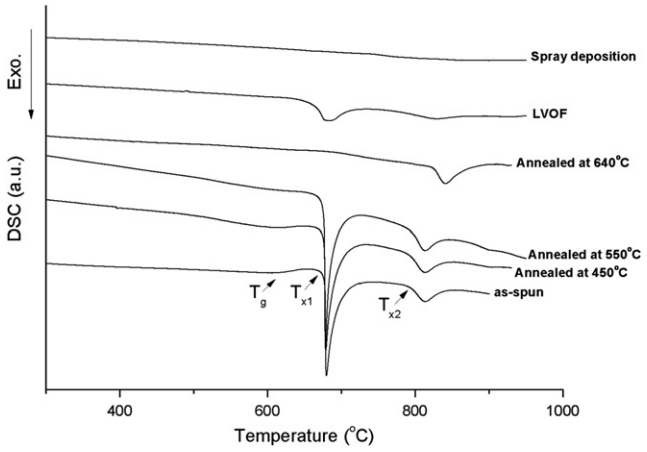

Fig. 2. DSC thermograms of the as-spun ribbons, annealed ribbons and coatings produced by LVOF and spray deposition routes.

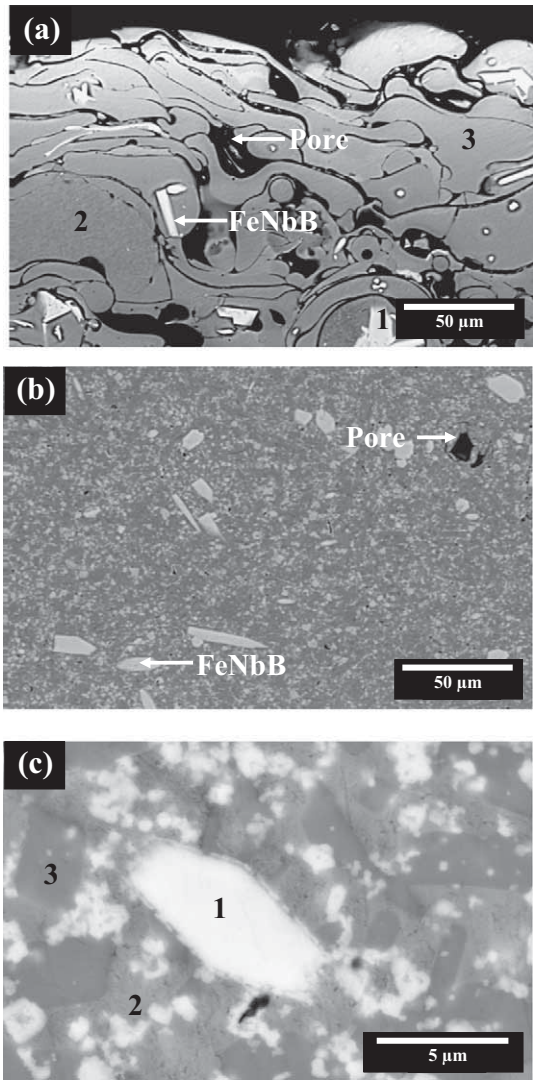

Fig. 3. Backscattered electron image of a cross-section of $Fe_{60}Cr_8Nb_8B_{24}$ coatings for: (a) LVOF process, (b) and (c) spray deposition route for different magnifications.

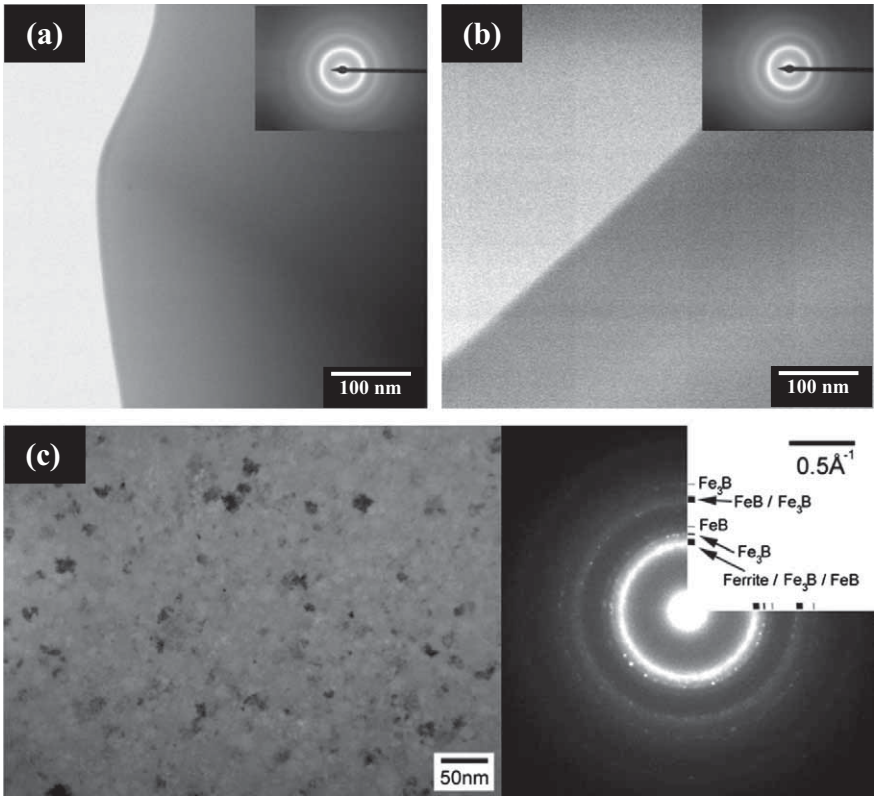

Fig. 4. Bright field (BF) TEM image and corresponding selected area electron diffraction (SAED) patterns for: (a) ribbons annealed at 450 °C, (b) ribbons annealed at 550 °C and (c) ribbons annealed at 640 °C.

The results hence point out a clear and widespread improvement of the corrosion properties for the amorphous alloys in comparison with the commercial FSS 430 in all studied media. This result is quite relevant since the commercial alloy has a much higher Cr content than the amorphous one (17.6 vs 8.0%, respectively).

Cr is the most important alloying element for the passivation of iron-based alloys so that this strong reduction in its concentration should in principle induce a much lower level of corrosion resistance in spite of the presence of Nb, an alloying element that has a positive effect in the corrosion resistance, in the ribbon composition. This can be seen as a strong evidence of the fact that superior corrosion properties must be ascribed in this case more to the amorphous structure than to the composition. Indeed, crystallization, even partial, appears to be deleterious to the corrosion resistance as it can be seen in Table 4: the ribbons annealed at 640 °C systematically showed higher corrosion current densities (up to two orders of magnitude) compared to the amorphous ribbons for all pH and particularly, lower corrosion resistance that the base FSS 430 system at alkaline media. The deleterious effect of even partial crystallization on the corrosion resistance comes first from the fact that any phase segregation, or just any surface heterogeneity as simple as different grain orientation is potentially a source of local galvanic coupling or passive film instability that can severely decrease corrosion resistance. Furthermore, in the present case, due to the alloy composition, the possible precipitation of Cr-rich and/or Nb-rich phases can be a factor of impoverishing the matrix exactly in those elements associated to the corrosion resistance. In this sense, amorphous materials ensure a highly homogenous composition and surface structure that eliminate or strongly reduce the presence of heterogeneities that trigger corrosion processes.

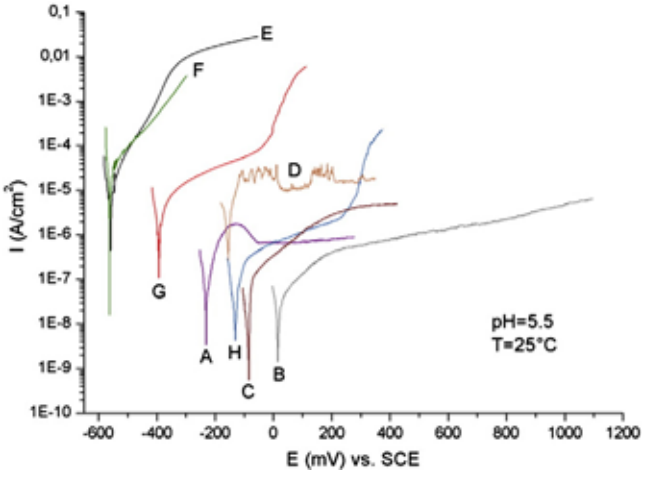

Fig. 5. Polarization curves at pH 5.5 and 25 °C for the $Fe_{60}Cr_8Nb_8B_{24}$ composition in the following conditions: as-spun ribbons (A), annealed ribbons at 450 °C (B), annealed ribbons at 550 °C (C), annealed ribbons at 640 °C (D) and coatings obtained by LVOF (E) and spray deposition (F), as indicated in the figure. The curves for a FSS 430 (G) and 316L SS (H) are included for comparison reason.

The same important improvement on corrosion resistance obtained for the amorphous ribbons was nevertheless not achieved for the coatings (spray deposition and LVOF) as also seen in Fig. 5 and Table 4. Indeed, for both coated samples there was no formation of the passive film, which resulted in lower corrosion potential and higher corrosion current densities with an active behavior upon anodic polarization, represented by the monotonic increase in the current density with the potential instead of reaching a passivation plateau as clearly seen in Fig. 5. It appears that the coating procedures did not bring any important improvement of the corrosion resistance which is shown to be lower than that of the FSS 430 for acid and alkaline pH and of the same order of magnitude in very acidic environment (pH = 3.0) for which the FSS 430 lost its passive character.

Table 4
Electrochemical properties obtained from the polarization curves for the as-spun ribbons, annealed ribbons and coatings produced by spray deposition and LVOF process. The values for a FSS 430 and 316L SS are included for comparison reason.

Composition ($Fe_{60}Cr_8Nb_8B_{24}$ at.%)	Media: pH = 10.0		Media: pH = 5.5		Media: pH = 3.0	
	E_{corr} (mV) vs. SCE	I_{corr} (μA/cm^2)	E_{corr} (mV) vs. SCE	I_{corr} (μA/cm^2)	E_{corr} (mV) vs. SCE	I_{corr} (μA/cm^2)
As-spun ribbon	−200 ± 10	0.16 ± 0.05	−230 ± 20	0.41 ± 0.01	−330 ± 30	0.16 ± 0.04
Ribbon annealed at 450 °C	−80 ± 10	0.30 ± 0.09	10 ± 2	0.30 ± 0.02	−420 ± 16	0.79 ± 0.05
Ribbon annealed at 550 °C	−100 ± 8	0.25 ± 0.05	−90 ± 5	0.25 ± 0.05	−30 ± 10	0.36 ± 0.04
Ribbon annealed at 640 °C	−220 ± 5	12 ± 7	−160 ± 5	8 ± 2	−130 ± 8	5.5 ± 0.5
Spray deposition	−500 ± 10	26 ± 1	−560 ± 10	35 ± 4	−610 ± 3	65 ± 7
LVOF	−550 ± 2	50 ± 9	−560 ± 7	20 ± 6	−560 ± 2	15 ± 5
FSS 430	−400 ± 30	2.5 ± 0.6	−390 ± 60	9 ± 1	−640 ± 20	70 ± 6
316L SS	−240 ± 30	0.26 ± 0.01	−140 ± 7	0.40 ± 0.01	−340 ± 10	0.44 ± 0.09

It is worth noticing that the higher current densities for the two coatings are nearest to the values obtained for the ribbons treated at 640 °C, the one containing the larger fraction of crystalline phases. The presence of crystalline phases seems to be the most important effect in the deterioration of the corrosion properties. In fact, in the coatings there is certainly an additional effect due to the presence of porosity; however, the corrosion properties were basically the same in the two types of coatings, despite the large variation in the porosity, from 2% (for the spray process) to 16% (for LVOF). It is interesting to notice the noisy behavior of the anodic polarization curve of the partially crystalline

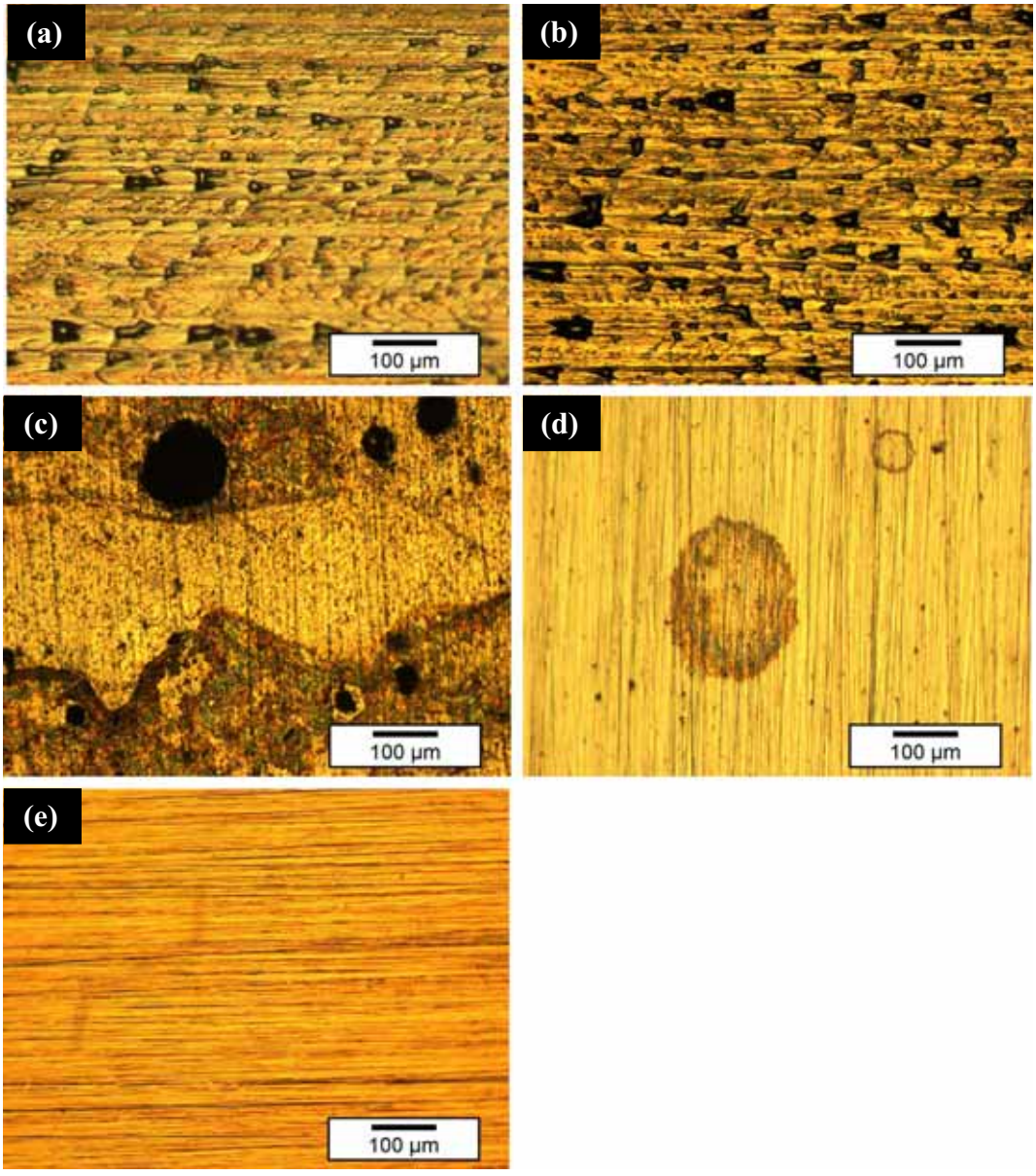

Fig. 6. Optical microscopy for: (a) as-spun ribbon before analysis; and for: (b) as-spun ribbons, (c) spray deposition coating, (d) FSS 430 and (e) 316L SS after polarization tests in pH = 5.5.

samples. The curve is characterized by some fast current spikes that can be associated to metastable pitting, or more probably in this case, to the selective dissolution, and hence local consumption of superficial crystallites [29,30]. The decrease of corrosion resistance in all tested conditions can be attributed to the formation of the α-Fe and Fe_xB (x = 1, 2, 3) crystalline phases that have greater corrosion susceptibility in comparison to that of the amorphous phases, promoting internal galvanic effects, selective dissolution and pitting in chloride-rich media. Considering that the Nb addition promotes an improvement in corrosion resistance attributed to the protective property of the niobium oxide film [26], we conclude that the feature of the FeNbB phase in the corrosion deterioration is not crucial in comparison with α-Fe and Fe_xB (x = 1, 2, 3).

OM images of the surfaces of the alloys after polarization tests in pH = 5.5 are shown in Fig. 6. The surface of the as-spun ribbon before and after immersion (Fig. 6a and b, respectively) shows some roughness due to melt spinning process which tend to align in the direction of copper wheel rotation, but no appreciable damage or pitting was observed after polarization analysis, indicating excellent corrosion resistance. However, the surface of the coatings of the same composition obtained by spray deposition process (Fig. 6c) reveal severe corrosion damage, probably related to the absence of passive film. Fig. 6d shows the presence of products of corrosion on the surface of the FSS 430 and clearly the corrosion resistance appears to be between the amorphous ribbons and the spray deposition coating. Fig. 6e shows that the 316L SS exhibit any visible pit or corrosion damage, maintaining a homogeneous surface implying that the high corrosion resistance can be attributed to the formation of a stable passive film.

The results indicate that for both general and localized corrosion behavior, the $Fe_{60}Cr_8Nb_8B_{24}$ amorphous alloys showed superior performance than the FSS 430 and equivalent to the highly resistant 316L stainless steel. The presence of chromium has been already shown to improve significantly the corrosion resistance of Fe-based metallic glasses [28], but it should be noted that the ribbons do not contain Mo and have a Cr content significantly lower than that of the 316L SS (8 vs. 18%, respectively) for a similar level of corrosion resistance. The amorphous $Fe_{60}Cr_8Nb_8B_{24}$ alloy was obtained by a rapid solidification method so that ideally it is single-phase, homogeneous material without any crystalline defects, which are susceptible to corrosion attack.

The general trends for the corrosion properties were basically the same in the three tested media; these trends suggest that the differences in the structure, which resulted from the different processes and in the present cases, in the presence of crystalline phases, have a crucial effect in the corrosion behavior and are more important than the porosity and exposed environment.

4. Conclusions

This work investigated the corrosion properties of the $Fe_{60}Cr_8Nb_8B_{24}$ alloy composition in the following conditions: as amorphous ribbons, as partially crystallized annealed ribbons and as coatings produced by spray deposition and LVOF routes. The corrosion properties were also measured, for reference, for the commercial FSS 430 and 316L SS.

The results showed that in both acidic and in alkaline media, the amorphous $Fe_{60}Cr_8Nb_8B_{24}$ ribbons have better corrosion resistance than the partially crystallized ribbons, coatings and FSS 430. The fully amorphous alloy also showed corrosion performance equivalent to that of the 316L SS.

The spray deposition and LVOF coatings did not show good corrosion behavior; the important deterioration in the corrosion properties was attributed to the presence of crystalline phases as observed for the partially crystallized ribbons.

Conflict of interest

There is no conflict of interest.

Acknowledgments

The authors gratefully acknowledge the financial support of the Brazilian institutions CAPES (BRAFITEC 047/07 and grant 048/2012), CNPq (304467/2009-0) and FAPESP (05/59594-0).

References

[1] B.L. Shen, A. Inoue, C. Chang, Appl. Phys. Lett. 85 (2004) 4911.
[2] S.J. Pang, T. Zhang, K. Asami, A. Inoue, Corros. Sci. 44 (2002) 1847.
[3] A. Inoue, A. Makino, T. Mizushima, J. Magn. Magn. Mater. 215–216 (2000) 246.
[4] A.L. Greer, K.L. Rutherford, I.M. Hutchings, Int. Mater. Rev. 47 (2002) 87.
[5] D. Zander, U. Koster, Mater. Sci. Eng. A 375–377 (2004) 53.
[6] A. Inoue, X.M. Wang, Acta Mater. 48 (2000) 1383.
[7] H.Y. Jung, S. Yi, Intermetallics 18 (2010) 1936.
[8] J. Cheney, K. Vecchio, Mater. Sci. Eng. A 492 (2008) 230.
[9] X. Wu, Y. Hong, Surf. Coat. Technol. 141 (2001) 141.
[10] Z. Zhou, L. Wang, F.C. Wang, H.F. Zhang, Y.B. Liu, S.H. Xu, Surf. Coat. Technol. 204 (2009) 563.
[11] P. Zhang, H. Yan, C. Yao, Z. Li, Z. Yu, P. Xu, Surf. Coat. Technol. 206 (2011) 1229.
[12] C. Zhang, R.Q. Guo, Y. Yang, Y. Wu, L. Liu, Electrochim. Acta 56 (2011) 6380.
[13] R.Q. Guo, C. Zhang, Q. Chen, Y. Yang, N. Li, L. Liu, Corros. Sci. 53 (2011) 2351.
[14] N. Sorensen, R. Diegle, ninth ed., Metals Handbook: Corrosion, vol. 13, ASME, New York, 1987. 864–870.
[15] D. Polk, B. Giessen, Overview of Principles and Applications, Chapter 1, Metallic Glasses, ASME, Metal Park, Ohio, 1978. 2–35.
[16] M. Telford, Mater. Today 7 (2004) 36.
[17] K. Hashimoto, M. Froment, Passivity of Metals and Semiconductors, Elsevier Science Publishers, Amsterdam, 1983. 235.
[18] S. Virtanen, H. Bohni, Corros. Sci. 31 (1990) 333.
[19] C.A.C. Souza, C.S. Kiminami, J. Non-Cryst. Solids 219 (1997) 155.
[20] M.F. Lopez, M.L. Escudero, E. Vida, A.R. Pierna, Electrochim. Acta 42 (1997) 659.
[21] C.A.C. Souza, F.S. Politi, C.S. Kiminami, Scr. Mater. 39 (1998) 329.
[22] C.A.C. Souza, M.F. Oliveira, J.E. May, W.J. Botta, N.A. Mariano, S.E. Kuri, C.S. Kiminami, J. Non-Cryst. Sol. 273 (2000) 282.
[23] C.A.C. Souza, C.S. Kiminami, J. ASTM Int. 7 (2010) 1.
[24] S. Pang, T. Zhang, K. Asami, A. Inoue, J. Mater. Trans. 42 (2001) 376.
[25] K. Leinartas, M. Samuleviciene, A. Bagdonas, R. Juskenas, E. Juzeliunas, Surf. Coat. Technol. 168 (2003) 70.
[26] C.S. Kiminami, C.A.C. Souza, L.F. Bonavina, L.R.P.A. Lima, S. Suriñach, M.D. Baró, C. Bolfarini, W.J. Botta, J. Non-Cryst. Sol. 356 (2010) 2651.
[27] X. Li, C. Qin, H. Kato, A. Makino, A. Inoue, J. Alloy Comp. 509 (2011) 7688.
[28] L. Wang, Y. Chao, Mater. Lett. 69 (2012) 76.
[29] T. Sourisseau, E. Chauveau, B. Baroux, Corros. Sci. 47 (2005) 1097.
[30] I.N. Bastos, S.S.M. Tavares, F. Dalard, R.P. Nogueira, Scr. Mater. 57 (2007) 913.